Journal of Computational Physics 227 (2008) 8636–8654

Contents lists available at ScienceDirect

Journal of Computational Physics

journal homepage: www.elsevier.com/locate/jcp

An immersed boundary method for smoothed particle hydrodynamics of self-propelled swimmers

S.E. Hieber, P. Koumoutsakos *

Chair of Computational Science, Universitatstrasse 6, ETH Zurich, CH-8092 Zurich, Switzerland

ARTICLE INFO

Article history:
Received 20 December 2007
Received in revised form 12 June 2008
Accepted 16 June 2008
Available online 27 June 2008

Keywords:
Particle Methods
Swimming
SPH
Immersed Boundary Methods

ABSTRACT

We present a novel particle method, combining remeshed Smoothed Particle Hydrodynamics with Immersed Boundary and Level Set techniques for the simulation of flows past complex deforming geometries. The present method retains the Lagrangian adaptivity of particle methods and relies on the remeshing of particle locations in order to ensure the accuracy of the method. In fact this remeshing step enables the introduction of Immersed Boundary Techniques used in grid based methods. The method is applied to simulations of flows of isothermal and compressible fluids past steady and unsteady solid boundaries that are described using a particle Level Set formulation. The method is validated with two and three-dimensional benchmark problems of flows past cylinders and spheres and it is shown to be well suited to simulations of large scale simulations using tens of millions of particles, on flow-structure interaction problems as they pertain to self-propelled anguilliform swimmers.

1. Introduction

The efficient and accurate simulation of fluid flows interacting with complex deforming geometries is of paramount importance to a number of scientific fields ranging from virtual surgery to biofluid dynamics. These simulations require flow solvers capable of handling accurately complex geometries and resolving efficiently the details of the flow field. In grid based methods a number of techniques, have been developed to address such problems distinguished by their handling of the solid geometry embedded in the flow field. Unstructured grid methods [15] are widely used techniques employing sets of grids that adapt to the deformation of the boundary. The advantages of these methods relies on the accuracy of the flow solver near boundaries and their flexibility in handling highly complex geometries. On the other hand, in particular for deforming geometries, these methods require an additional computational cost for constructing the grid anew at each time step and they are often associated with an additional computational overhead in solving the governing equations due to the non-uniformity of the associated mesh. Immersed Boundary Methods (IBM), pioneered by Peskin [39], use a straightforward boundary representation along with structured grids to discretize flows past complex deforming geometries without constructing the grid anew at each time step. In IBM the effects of the boundary are accounted for by introducing a forcing term on the governing equations localized at the boundary of the body. These methods have attracted significant attention in recent years for the simulation of complex flows in two and three-dimensions (see [34] and references therein).

Particle methods such as Vortex Methods (VM) and Smoothed Particle Hydrodynamics (SPH) are Lagrangian techniques that are widely considered as being capable of handling flows past complex deforming geometries. In fact we note that the original development of Immersed Boundary Methods was in the context of VMs [39] for the simulation of heart leaflets at physiological Reynolds numbers. Building on the viscous VM introduced by Chorin [6], Peskin's

* Corresponding author. Tel.: +41 44 632 5258; fax: +41 44 632 1703.
E-mail addresses: simone_elke.hieber@alumni.ethz.ch (S.E. Hieber), petros@ethz.ch (P. Koumoutsakos).

0021-9991/$ - see front matter © 2008 Elsevier Inc. All rights reserved.
doi:10.1016/j.jcp.2008.06.017

pioneering simulations, coupled IBM and VM in an effort to use a minimal set of computational points to capture the dynamics of the vorticity field in a complex deforming geometry. These simulations however were hindered at that time by the quadratic cost of VMs and by the low accuracy associated with their treatment of viscous effects. Another issue, hidden in the Lagrangian description of the flow, is the inaccuracy of particle methods when the flow distorts the computational elements. The fact that VMs were able to provide reasonable estimates of force fields and flow structures (in particular in 2D), but they were not capable of Direct Numerical Simulations of bluff body flows, detracted from their original success. Recent works introducing a regularization of the particle locations have rekindled and interest in these methods as being capable of performing Direct Numerical Simulations (see [29] and references therein), albeit only for flows past relatively simple boundaries.

Contemporary to the inception of VMs [6,31], Lucy [33] and Gingold and Monaghan [17] introduced the method of Smoothed Particle Hydrodynamics to discretize the velocity–pressure formulation of the compressible Navier–Stokes equations. A key advantage of SPH is the avoidance of solving an elliptic problem to determine the velocity field of the flow by introducing a state equation linking the pressure and the density field of the flow. Over the years a large body of work has implemented SPH for simulations of flows ranging from astrophysics, to polymer dynamics (see the review by Monaghan [36] and references therein). The SPH method is inherently adaptive as particle attributes (strength, locations) evolve according to their material time derivatives. At the same time, the particle distortion, associated with all Lagrangian particle methods, often leads to large inaccuracies of the quantities that are been simulated. In order to circumvent this problem a consistent framework involving remeshing of particle locations using moment conserving schemes was introduced in [30]. The moment conserving remeshing schemes developed in [27], were inspired in fact by SPH interpolations [17], and they have been in turn applied in the context of SPH resulting in the method of remeshed SPH (rSPH) [5]. In the rSPH the particles are reinitialized (remeshing) on a regular grid and the new particle strengths are adjusted so that the moments of the field quantities are conserved. We emphasize that the combination of meshes and particle does not detract from the adaptive character of the method as the nonlinear convection term is still described in a Lagrangian fashion. Care must be exercised however when remeshing near boundaries so as not to introduce spurious structures while conserving the moments of the flow. This remeshing difficulty can be overcome by combining Immersed Boundary Methods and the rSPH as shown in this work.

In IBM the effects of the boundary to the flow are accounted for by adding a forcing term to the governing equations [40,42,41]. This forcing term is computed so as to enforce the no-slip boundary condition on the surface of the body. The equations are usually discretized on an Eulerian grid which does not need to coincide with the location of the body and a forcing term has to be computed on the grid nodes in the vicinity of the boundary. Fadlun et al. [14] proposed an IBM for finite-difference methods where the velocity field for grid points near the boundary is interpolated linearly from values at the boundary leading to a second order accuracy for the overall method. Kim [26] presented a similar approach for finite-volume methods combined with a mass source to increase the accuracy of the simulations.

These approaches have been so far mostly limited to Eulerian methods for incompressible flows. In the context of particle methods recent works by Cottet and Maitre [10] and Morgenthal and Walther [37] combined VMs with immersed interface and immersed boundary methods. Furthermore the IBM technique has been coupled with the Reproducing Kernel Methods [49] while in [12] Immersed Boundary techniques were combined with Lattice Boltzmann simulations.

In this work we present a novel particle Immersed Boundary method for simulations using remeshed Smoothed Particle Hydrodynamics *(rSPH-IB)*. The geometry of the body is described by Lagrangian particle level sets [21] and a forcing term is evaluated on the boundary points such that the no-slip boundary condition on the body is fulfilled. The extrapolation of the forcing term onto the neighboring particles employs a high-order B-Spline kernel. The method is applied to simulations of flows of self-propelled anguiliform swimmers. In this flow-structure interaction problem the fluid forces are taken into account in order to determine the translation and rotation of the body. Anguilliform swimmers propel themselves by undulations that propagate along the entire length of the body and their simulation requires the continuous adaptation of the computational elements that describe the flow field. This is precisely the scope of the proposed method and we compare our result with related simulations [25] employing finite volume discretisations.

The paper is organized as follows. First, we present the governing equations in Section 2 and discuss the particle representation of Immersed Boundaries in Section 3. In Section 4, we demonstrate the performance of the rSPH-IB method on Poiseuille flow, flow past a circular cylinder and sphere. We compare the characteristic numbers of the flow for various Reynolds numbers with experimental and numerical results presented in the literature. Section 5 involves the simulation of fluid-structure interactions describing a self-propelled swimmer. We conclude in Section 6 and discuss advantages and limitations of the present approach and outline future work.

2. Governing equations

We consider the isothermal, compressible Navier–Stokes equations, described in a non-dimensional Lagrangian, velocity–pressure framework as

$$\frac{\mathrm{D}\rho}{\mathrm{D}t} = -\rho \nabla \cdot \mathbf{u}, \tag{1}$$

$$\rho \frac{\mathrm{D}\mathbf{u}}{\mathrm{D}t} = -\frac{1}{\mathrm{M}^2\gamma}\nabla p + \frac{1}{Re}\nabla \cdot \boldsymbol{\tau}, \tag{2}$$

$$\tau_{ij} = \mu\left(\frac{\partial u_i}{\partial x_j} + \frac{\partial u_j}{\partial x_i} - \frac{2}{3}\delta_{ij}\frac{\partial u_k}{\partial x_k}\right) \tag{3}$$

where $\frac{\mathrm{D}\diamondsuit}{\mathrm{D}t} = \frac{\partial \diamondsuit}{\partial t} + (u \cdot \nabla)(\diamondsuit)$ denotes the material derivative, ρ denotes the density, u the velocity, p the pressure, τ the shear stress tensor with the elements τ_{ij}, x_i are the components of the position, u_i the components of the velocity where Einstein's summation convention must be taken into account. The Reynolds number Re of the flow is defined as

$$Re = \frac{\rho_0 U d}{\mu}, \tag{4}$$

where ρ_0 is the characteristic density of fluid, U the characteristic velocity, μ the dynamic viscosity and d is the characteristic length of the boundary. The Mach number M is the ratio of the characteristic velocity U to the speed of sound c_0

$$M = \frac{U}{c_0} = \frac{U}{\sqrt{RT_0}}. \tag{5}$$

The system of differential equations Eqs. (1)–(3) is closed by introducing equation of state for an ideal gas

$$p = \rho T \tag{6}$$

where T is the temperature. In the present work we assume the temperature $T = T_0$ to be constant in space and time.

The initial condition of the flow is described by a density and a velocity field. The no-slip boundary condition is translated into a body force for the fluid in the *vicinity* of the body in the context of the *immersed* boundary technique. The inflow boundary involves a prescribed inlet velocity and a homogenous Neumann boundary condition for the pressure. At the outlet, we prescribe the pressure field and use a homogenous Neumann boundary condition for the velocity. Periodic boundary conditions are employed in the remaining boundaries of the computational domain.

3. Re-meshed particle methods and immersed boundaries

3.1. Function and gradient approximations using particles

In the context of particle methods [18,8] a smooth approximation of a function $\Phi(\mathbf{x})$ is constructed by using a mollification kernel $\zeta_\epsilon(\mathbf{x})$:

$$\Phi_\epsilon(\mathbf{x}) = \Phi \bigstar \zeta_\epsilon = \int \Phi(\mathbf{y})\zeta_\epsilon(\mathbf{x}-\mathbf{y})\mathrm{d}\mathbf{y} \tag{7}$$

where ϵ denotes a characteristic length of the kernel.

The mollification accuracy of this kernel is of order r when the following moment conditions [8] are satisfied:

$$\int \zeta_\epsilon(\mathbf{x})\mathrm{d}\mathbf{x} = 1, \tag{8}$$

$$\int \mathbf{x}^i \zeta_\epsilon(\mathbf{x})\mathrm{d}\mathbf{x} = 0 \quad \text{if } |\, i \,| \leqslant r-1, \tag{9}$$

$$\int |\, \mathbf{x} \,|^r \zeta_\epsilon(\mathbf{x})\mathrm{d}\mathbf{x} \leqslant \infty. \tag{10}$$

This mollified approximation $\Phi_\epsilon(\mathbf{x})$ is discretised using the particle locations as quadrature points and a particle approximation of the regularized function is

$$\Phi^h_\epsilon(\mathbf{x}) = \Phi^h \bigstar \zeta_\epsilon = \sum_{p=1}^{N} v_p \Phi_p \zeta_\epsilon(\mathbf{x}-\mathbf{x}_p), \tag{11}$$

where $\mathbf{x}_p$, and v_p denote the position and volume of the pth particle, and $\Phi_p = \Phi(\mathbf{x}_p)$ the value at the $p = 1, \cdots, N$ particle locations.

The error introduced by the quadrature of the mollified approximation of Φ can be distinguished in two parts [8] as

$$\Phi - \Phi^h_\epsilon = (\Phi - \Phi \bigstar \zeta_\epsilon) + (\Phi - \Phi^h) \bigstar \zeta_\epsilon. \tag{12}$$

The first term in Eq. (12) denotes the mollification error that can be controlled by appropriately selecting the kernel properties. The second term denotes the quadrature error due to the approximation of the integral on the particle locations. The overall accuracy of the method [8] results in

$$\|\Phi - \Phi^h_\epsilon\|_{0,p} \leqslant \|\Phi - \Phi_\epsilon\|_{0,p} + \|\Phi_\epsilon - \Phi^h_\epsilon\|_{0,p} \sim \mathcal{O}(\epsilon^r) + \mathcal{O}\left(\frac{h^m}{\epsilon^m}\right), \tag{13}$$

where $\|(.)\|_{0,p} = (\int (.)^p d\mathbf{x})^{1/p}$ and r denotes the order of the first *non-vanishing* moment of the kernel ζ_ϵ [8]. For equidistant particle locations $m = \infty$ and for positive kernels such as the Gaussian, $r = 2$. Here for ζ_ϵ a quartic spline kernel with second order of accuracy is implemented

$$\zeta_\epsilon(\mathbf{x}) = n_d \overline{\zeta_\epsilon} = n_d \begin{cases} \frac{s^4}{4} - \frac{5s^2}{8} + \frac{115}{192} & 0 \leqslant s < \frac{1}{2}, \qquad s = \frac{|\mathbf{x}|}{\epsilon}, \\ -\frac{s^4}{6} + \frac{5s^3}{6} - \frac{5s^2}{4} + \frac{5s}{24} + \frac{55}{96} & \frac{1}{2} \leqslant s < \frac{3}{2}, \\ \frac{(2.5-s)^4}{24} & \frac{3}{2} \leqslant s < \frac{5}{2}, \\ 0 & s \geqslant \frac{5}{2}. \end{cases} \tag{14}$$

The normalization value n_d depends on the dimension of the problem and is computed as

$$n_d = \frac{1}{\sum_j v_j \overline{\zeta_\epsilon}(\mathbf{x} - \mathbf{x}_j)} \tag{15}$$

ensuring the property of *partition of unity* for the particles. Kernels of arbitrary order [1] are possible by giving up the positivity of the kernel function. Note that the moment conditions expressed by the integrals of the mollifier functions are not often well represented in the case of discrete particle sets but the moment conditions can be ensured by appropriate normalisations [8].

The error estimates reveal a very important fact for smooth particle approximations. In order to obtain accurate approximations of the discretized quantities, *smooth particles must overlap*. This fact must be taken into account when considering particle simulations with Lagrangian adaptivity as the flow map often results in distortion of the computational elements, thus making the simulations inaccurate. This observation leads to the requirement for a regularization of the particle locations which in turn may seem as detracting from the adaptive character of the method. As it is noted below this is not the case as the regularization of the particle locations can be achieved by introducing less error than that introduced by particle mollification by appropriately conserving the moments of the flow field.

3.2. Remeshing

A key aspect of the present method involves the a remeshing procedure. In smooth particle methods, as discussed earlier, particles must overlap at all times in order to guarantee the convergence of the method [9]. As it is shown in [7] remeshing is equivalent to a regularisation of the advected quantities.

In this work remeshing is employed in order to regularize the distorted particle locations and to redistribute particle quantities accordingly onto a uniform set of particles with the spacing h.

The redistribution of particle quantities is achieved using the 3rd order $M'4$ kernel [28] which in one dimension is expressed as

$$M'_4(x,h) = \begin{cases} 1 - \frac{5s^2}{2} + \frac{3s^3}{2} & 0 \leqslant s < 1, \qquad s = \frac{|x|}{h} \\ \frac{(1-s)(2-s)^2}{2} & 1 \leqslant s < 2, \\ 0 & s \geqslant 2. \end{cases} \tag{16}$$

In higher dimensions the interpolation formulas are tensorial products of their one-dimensional counterparts. This remeshing kernel is used in order to redistribute on regularised particle locations the discretized extensive properties (here mass and momentum) of the field that need to be conserved.

In the context of SPH, remeshing requires a normalization scheme of the remeshed quantities in terms of the particle volumes. The normalization scheme is similar to the normalization that ensures the partition of unity (Eq. (15)).

$$\Phi_{j,\mathrm{new}} = \frac{V_{\mathrm{new}}}{\sum_{i=1}^{N_{\mathrm{old}}} V_{\mathrm{old}} M'4(|\, x_i - x_j \,|, h)} \sum_{i=1}^{N_{\mathrm{old}}} \Phi_{i,\mathrm{old}} M'4(|\, x_i - x_j \,|, h), \tag{17}$$

where $V_{\mathrm{new}} = h^3$ is the volume of the new particle.

After remeshing the new regularized particles are ready to be advected with the flow field. We note that this method does not detract from the Lagrangian character of the method as the remeshing step is only seen as a regularization step for the particle locations that are always advected by the flow map.

3.2.1. Particle derivative approximations

Particle approximations of the derivative operators can be constructed through their integral approximations. This can be achieved by taking the derivatives of Eq. (7) as convolution and derivative operators commute in unbounded or periodic domains. This approximation is often employed in SPH [35] where derivatives of a field quantity Φ on a particle p are approximated in a conservative form as

$$\left\langle \frac{\partial}{\partial x_i}\Phi \right\rangle_p = \sum_q v_q(\Phi_q - \Phi_p)\frac{\partial}{\partial x_i}\zeta_\epsilon(\mathbf{x}_p - \mathbf{x}_q), \tag{18}$$

$$\left\langle \frac{\partial}{\partial x_i x_j}\Phi \right\rangle_p = \sum_q v_q(\Phi_q - \Phi_p)\frac{\partial}{\partial x_i x_j}\zeta_\epsilon(\mathbf{x}_p - \mathbf{x}_q), \tag{19}$$

where v_q is the volume of particle q. The normalization values $n_{d,1}, n_{d,2}$ of $\frac{\partial}{\partial x_i}\zeta_\epsilon(\mathbf{x}) = n_{d,1}\frac{\partial}{\partial x_i}\overline{\zeta_\epsilon}(\mathbf{x})$ and $\frac{\partial}{\partial x_i x_j}\zeta_\epsilon(\mathbf{x}) = n_{d,2}\frac{\partial}{\partial x_i x_j}\overline{\zeta_\epsilon}(\mathbf{x})$ are chosen such that the corresponding non-zero moment condition [13] is *satisfied*. The kernel of Eq. (14) has its first three derivatives continuous allowing a smooth approximation of the spatial derivatives of $\Phi(\mathbf{x})$. The computation of the right hand side of the ODEs employs these formulas for the computation of derivatives as defined in Eqs. (1)–(3). An alternative formulation involves the development of integral operators that are equivalent to differential operators [13] as they were first introduced for the integral approximation of the Laplacian [11] in the diffusion equation.

3.3. An immersed boundary method for remeshed SPH

In rSPH-IB, (Fig. 1), a forcing term f is added to the momentum equation (Eq. (2)) such that the no-slip condition is satisfied on the boundary.

$$\rho\frac{\mathrm{D}u}{\mathrm{D}t} = -\frac{1}{\mathrm{M}^2\gamma}\nabla p + \frac{1}{Re}\nabla\cdot\tau + f. \tag{20}$$

We approximate the material derivative by a differential quotient:

$$\rho_i\frac{u_{i+1} - u_i}{\Delta t} = -\frac{1}{\mathrm{M}^2\gamma}\nabla p_i + \frac{1}{Re}\nabla\cdot\tau_i + f_i \tag{21}$$

Solving for f_i and assuming we reach the desired velocity within this time step ($u_{i+1} = u_{\text{desired}}$) yields

$$f_i = \rho_i\frac{u_{\text{desired}} - u_i}{\Delta t} - \left(-\frac{1}{\mathrm{M}^2\gamma}\nabla p_i + \frac{1}{Re}\nabla\cdot\tau_i\right). \tag{22}$$

The forcing term f acts locally on the boundaries where a no-slip condition is imposed and the velocity u_{desired} is known. We note that for the simulations past stationary boundaries, conducted in this study, the dominant contribution (90%) to the forcing term is due to the first term of Eq. (22), "correcting" the spurious velocity field at the boundary.

The boundary is described by boundary points associated in turn with an impact zone in the flow domain as determined by the particle-mesh interpolations necessary for the transfer of the forcing term between the fluid and the body (Fig. 1). We employ a kernel based on B-Splines for a dirac delta approximation of the forcing term f. We rely on particle-mesh and mesh-particle interpolations, similar to those employed for remeshing in order to transport quantities between the fluid particles and the boundary.

Our implementation involves the separation of the forcing term into two parts:

$$f_i = \rho_i(f_{ip} + f_i b) \tag{23}$$

$$f_{ip} = \frac{-u_i}{\Delta t} - \frac{1}{\rho_i}\left(-\frac{1}{\mathrm{M}^2\gamma}\nabla p_i + \frac{1}{Re}\nabla\cdot\tau_i\right) \tag{24}$$

$$f_{ib} = \frac{u_{\text{desired}}}{\Delta t} \tag{25}$$

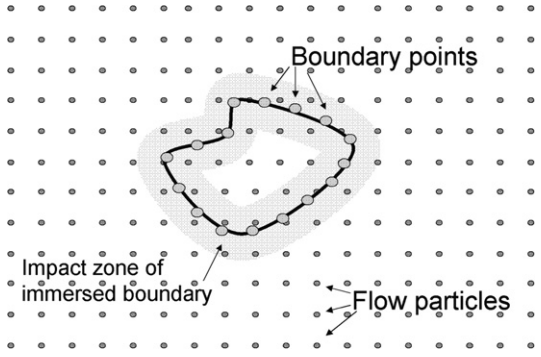

Fig. 1. Particle Immersed Boundary Method. The immersed boundary is discretized using boundary points that can only impact flow particles within the kernel support.

The rSPH-IB method consists the following steps:

1. Evaluation of the first part of the forcing term f_{ip} on the particle
2. Interpolation of f_{ip} from the particles onto the boundary points via mesh.
3. Evaluate forcing term f_i on the boundary points by adding f_{ib}
4. Interpolation of forcing term f from the boundary points to the particles via mesh.
5. Evolving particles according to the governing equations including forcing term f.

This approach tends to exhibit small scale oscillations in the pressure profile at complex boundaries. These oscillations can be limited by the adjustment the density in the vicinity of the body. In this context, the ghost particles reside at the boundary and their density is here chosen to be the averaged density of the neighboring fluid particles within their support.

3.4. Particle equations

The particle position $\mathbf{x}_p$, mass m_p, volume v_p, and velocity component $\mathbf{u}_{i,p}$ evolve by the following system of ordinary differential equations derived from Eqs. ((1)–(3))

$$\begin{aligned}
\frac{\mathrm{d}\mathbf{x}_p}{\mathrm{d}t} &= \mathbf{u}_p \\
\frac{\mathrm{d}m_p}{dt} &= 0 \\
\frac{\mathrm{d}v_p}{\mathrm{d}t} &= \langle \nabla \cdot \mathbf{u} \rangle_p v_p \\
\frac{\mathrm{d}\mathbf{u}_{i,p}}{\mathrm{d}t} &= \frac{v_p}{m_p}\left(-\frac{1}{\mathrm{M}^2\gamma}\langle \frac{\partial p}{\partial x_i} \rangle_p + \frac{1}{Re}\langle \frac{\partial \tau_{ij}}{\partial x_j} \rangle_p \right) + f_{i,p}
\end{aligned} \tag{26}$$

where $\langle \diamond \rangle_p$ denotes the derivative approximation on a particle p (cf. Eq. (18)) and

$$\left\langle \frac{\partial \tau_{ij}}{\partial x_j} \right\rangle_p = \mu \left(\left\langle \frac{\partial^2 u_i}{\partial x_k^2} \right\rangle_p + \frac{1}{3} \left\langle \frac{\partial^2 u_l}{\partial x_i \partial x_l} \right\rangle_p \right) \tag{27}$$

$$p_p = \frac{m_p}{v_p} T_0 \tag{28}$$

In the present study, the Laplacian approximation $\left\langle \frac{\partial^2 u_i}{\partial x_k^2} \right\rangle_p$ is evaluated using the particle strength exchange approach [11].

$$\left\langle \frac{\partial^2 u_i}{\partial x_k^2} \right\rangle_p = \sum_p v_p (\mathbf{u_{i,p}} - \mathbf{u_{i,q}}) \nabla^2 \zeta_\epsilon (\mathbf{x}_q - \mathbf{x}_p) \tag{29}$$

$$\zeta_\epsilon = \frac{15}{\epsilon^{-3}\pi} \frac{1}{|x|^{10} + 1} \tag{30}$$

The second order kernel ζ_ϵ was successfully applied in simulations of diffusion in complex geometries [47].

The interface between the body and the fluid is captured using the Particle Level Set Method [21,20]. The level set function represents the signed distance function to the interface. The particles carry the level set information as a scalar attribute Φ_p that remains constant during the time integration:

$$\frac{\mathrm{d}\Phi_p}{\mathrm{d}t} = 0 \tag{31}$$

We reinitialize the level set value based on the prescribed deformation of the geometry after every remeshing to maintain the signed distance property. The exact knowledge of the body shape allows the reinitialization of the level set function with its analytical value. We note that the use of the Level Set formulation enables the extension of the method to complex deforming geometries that may even undergo topological changes that is of interest to virtual surgery applications.

The inlet and outlet boundary conditions are imposed by using image particles that have similar physical properties as the flow particles. The boundary particles interact with the flow particles such that the boundary conditions are satisfied. The no-slip boundary condition on the body surface is handled by the proposed particle Immersed Boundary Method.

The implementation is embedded into the framework of the Parallel Particle-Mesh Library (PPM) [47] to perform large-scale simulations on massively parallel computer architectures.

4. Results

We implement the proposed rSPH-IB method on simulations of several benchmark flow problems, and present results such as drag coefficient and vorticity isosurfaces. We discuss the advantages and drawbacks of the present method and

we demonstrate its capabilities in capturing flows past unsteady deforming geometries in simulations of flows past a self-propelled anguilliform swimmer.

The flows are characterized by their Reynolds and Mach numbers as defined in Section 2. The drag and lift coefficient are defined as

$$(C_d, C_L) = \frac{(F_D, F_L)}{0.5\rho U^2 A}, \tag{32}$$

where F_D, F_L, demote the drag and lift force respectively on the body and A denotes the reference area. The Strouhal number is defined as the dimensionless frequency of the shedding vortices

$$St = \frac{fd}{U}, \tag{33}$$

where f is the vortex shedding frequency, obtained using the Fast Fourier Transform of the lift coefficient.

In order to perform effectively incompressible simulations, we have kept the Mach number to a minimum. On the other hand, the low Mach number dictates a small time step for integrating the governing equations. We have chosen the Mach number empirically so as to have a compromise between these two objectives.

4.1. Poiseuille flow

In order to verify the capability of the present method to capture flows past solid boundaries we consider first the Poiseuille flow. We note that this flow is a rather trivial example, in the context of grid based methods, but serves to demonstrate that the proposed particle-mesh framework allows for a straightforward simulation of such flows. The 2D simulation domain was considered to be a unit square with periodic boundary condition at the inlet/outlet boundary (x = 0, x = 1) and no-slip conditions at the plates (y = 0, y = 1). We consider a fluid density with an initial density of $\rho = \rho_0 = 1$ at a Reynolds number of $Re = 100$ and a Mach number of $M = 0.5$. The fluid is initially at rest and accelerated by a constant pressure gradient of 0.001. We employ a 2nd order Runge Kutta scheme with a time step of $\delta t = 0.0005$ in all cases. For the error analysis the maximal difference in the velocity profile to the analytical solution is evaluated when the profile becomes stationary at time $T = 70$. The error normalized by the maximal velocity is shown in Fig. 2. The error analysis shows that the present method exhibits second order accuracy in space.

4.2. Flow past a cylinder

We present simulations of flow past a cylinder for various Reynolds numbers using the proposed rSPH-IB in order to demonstrate the capability of the method to capture flows past non grid conforming boundaries and to compare the results of our simulations with the related, benchmark experimental and computational investigations [19,26,32,38,45,48,50].

We use a 4th order Runge Kutta scheme for time integration with constant time step of $\Delta t = 0.001$. The domain size is set to $15d \times 30d$ where d is the diameter of the cylinder. The Mach number M is 0.05 The solution is remeshed after every time step. A particle spacing of $h = 0.078d$ for $Re = 100$ and $h = 0.052d$ for $Re = 1000$ is employed in the reported simulations. The fluid is initially at rest and accelerated by a small artificial force until the desired inlet velocity is reached to avoid the development of pressure waves at the boundary. The shedding is induced by a perturbation of the inlet velocity in the lateral

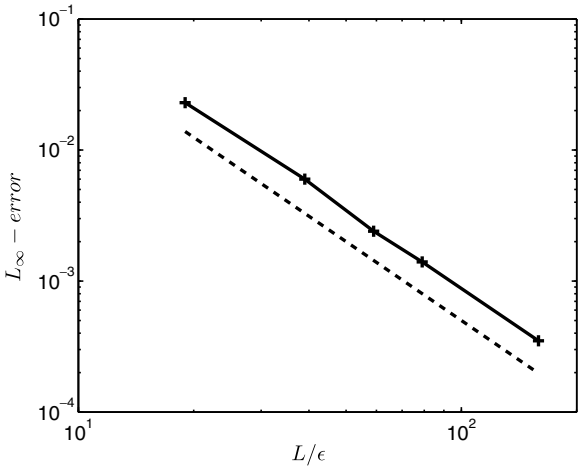

Fig. 2. Poiseuille flow: $L_\infty-$ error velocity of the particle Immersed Boundary Method (rSPH-IB) compared to second order scaling (dashed line).

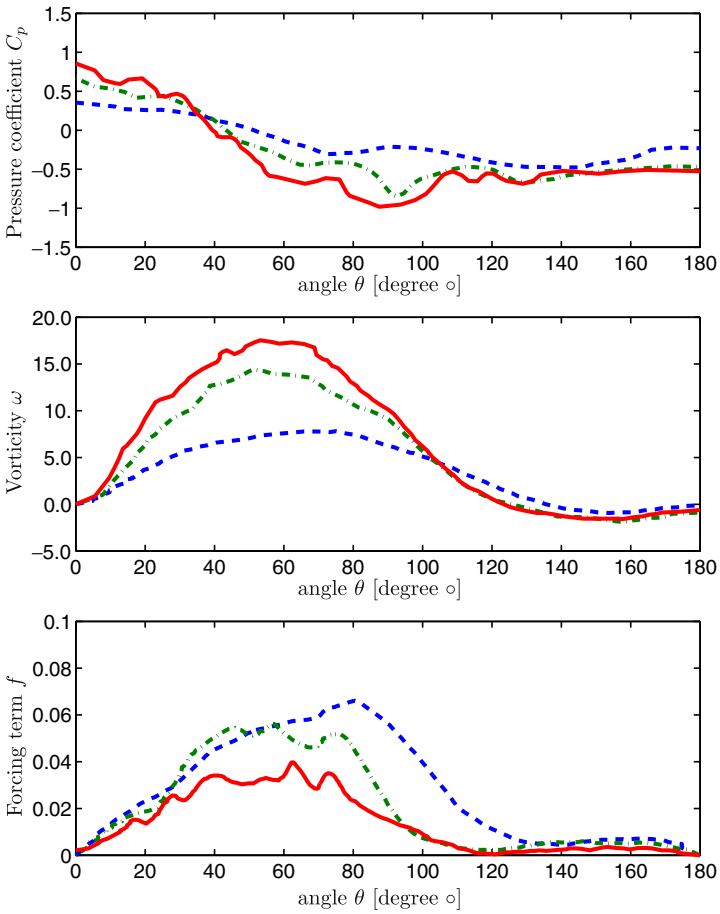

Fig. 3. Flow past a cylinder at $Re = 100$: Effect of the resolution on wall quantities at $t = 2.5$ before flow perturbation. The dashed, dash-dotted and solid lines represent particle spacings of $h = 0.156d$, $h = 0.078d$ and $h = 0.039d$, respectively.

direction as described by Ploumhans [44]. Fig. 3 shows the pressure coefficient, the vorticity and the forcing term along the boundary for three resolutions. In the region of high vorticity a high resolution is required to capture the boundary effects. This region also reflects a high forcing term. Furthermore we note the correlation of the forcing term with the the pressure gradient and the wall vorticity. Using Richardson's extrapolation for the Euclidian norm of the wall vorticity we find that the method converges with an order of 1.82.

Figs. 4 and 5 shows the vorticity field at $Re = 100$ and $Re = 1000$ respectively. These vorticity fields match qualitatively well with the respective vorticity fields obtained via Finite Element solutions by Singh et al. [48].

Fig. 6 shows the variation of the drag coefficient with the Reynolds number. The simulation results of the rSPH-IB method are compared with experimental results [45] and incompressible flow computations. We observe that the drag coefficient and Strouhal frequency values from present computations match well the experimental values for $Re < 200$

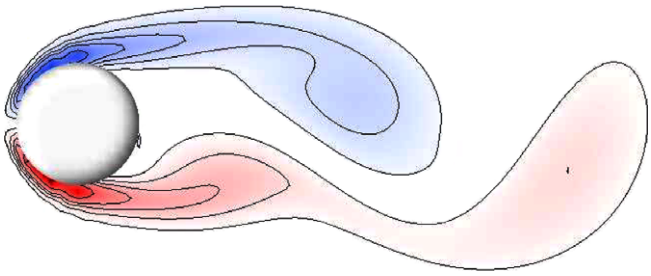

Fig. 4. Flow past a cylinder at $Re = 100$. Contour levels of the vorticity contours at $(\pm 20, \pm 15, \pm 10, \pm 7.5, \pm 5, \pm 2.5)$.

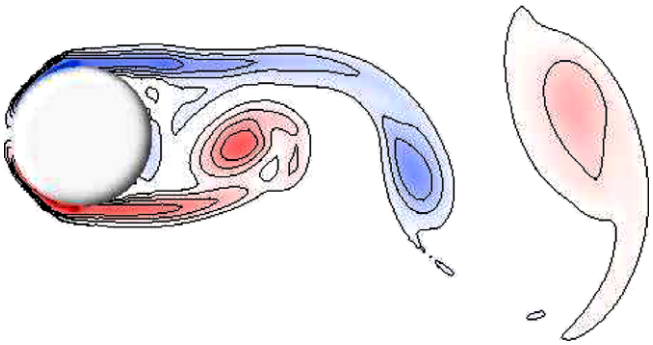

Fig. 5. Flow past a cylinder at $Re = 1000$. Contour levels of the vorticity contours at $(\pm 20, \pm 15, \pm 10, \pm 5)$.

and previous simulation results as listed on Table 1. Beyond $Re = 180$ the wake flow undergoes three-dimensional transitional instabilities. For $Re > 200$ the drag coefficient and the Strouhal number are overpredicted by the two-dimensional computations.

Fig. 7 shows the pressure coefficient of the time averaged flow along the cylinder surface for $Re = 100$ compared to the result of Park et al. [38]. The angle θ is measured clockwise from the front stagnation point of the cylinder. The pressure coefficient C_p agrees well with the results of Park et al. [38]. The pressure field is noisy for angles $10^\circ < \theta < 50^\circ$ due to unresolved pressure waves in the compressible fluid.

Fig. 8 shows that the computational cost of the method scales linearly with the number of particles.

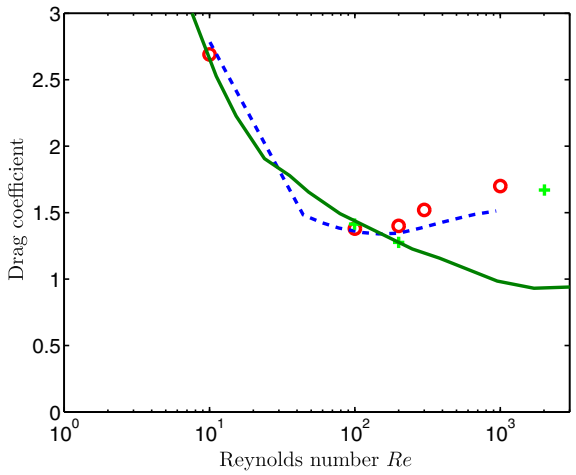

Fig. 6. Flow past a cylinder: Time averaged drag coefficient of rSPH-IB (circles) versus Reynolds number in comparison with experimental data (solid line, taken from Ref. [45]), a Spectral Method (dashed line, taken from Ref. [48]) and a FEM solution (crosses) [48].

Table 1
Flow past a cylinder: comparison with previous simulations and experiments

$Re = 100, D = 0.2$	Drag coefficient	Strouhal number
rSPH-IB	1.38	0.162
Henderson [19]	1.35	–
Park et al. [38]	1.33	0.165
Silva et al. IBM [32]	1.39	0.162
Singh et al. FEM [48]	1.41	0.164
Kim et al. FV IBM [26]	1.33	0.165
Wieselberger (Exp.) taken from Ref. [45]	1.45	–
Williamson (Exp.) [50]	–	0.165

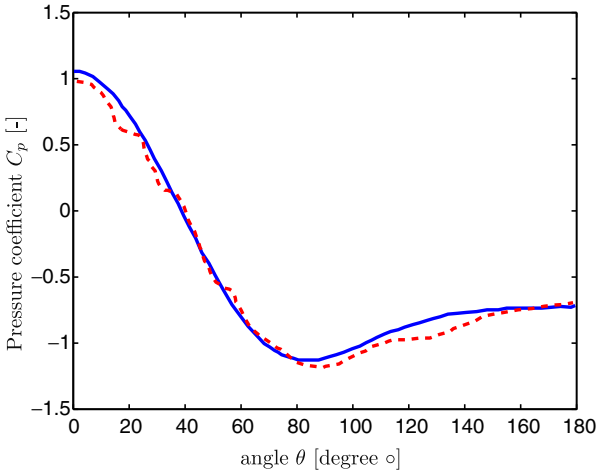

Fig. 7. Flow past a cylinder at $Re = 100$: Pressure coefficient C_p (dashed line) versus angle in comparison with the solution of Park [38] (solid line).

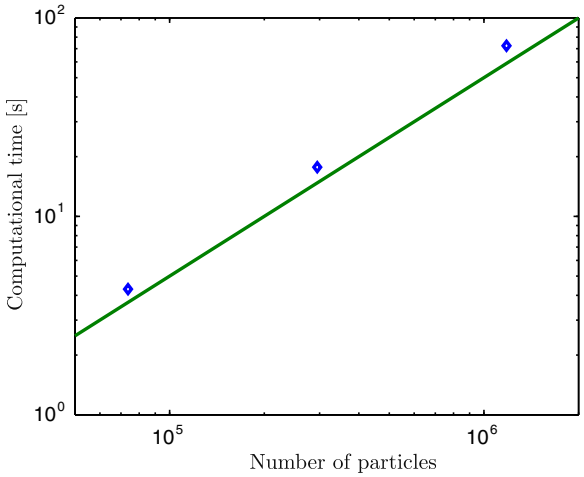

Fig. 8. Effect of the resolution on computational effort per integration step (Runge Kutta 4) on 4 processors. The solid line represents linear scaling.

4.3. Flow past a sphere

In order to assess the capability of the present method to simulate flows past three-dimensional geometries we simulate the flow past a sphere at $M = 0.1$ and $Re = 100$ and $Re = 300$. Wakes of incompressible fluid behind spheres are observed to be steady for Reynolds numbers below 270. Above this limit vortices break off and are periodically shed to form chain linked vortex loops. Table 2 shows that the drag and lift coefficient of the rSPH-IB method compare well with the results of simu-

Table 2
Flow past a sphere: Comparison with previous simulations

$Re = 100$	Drag coefficient	Lift coefficient	Strouhal number
rSPH-IB (M=0.1)	1.15	–	–
Fornberg [16]	1.09	–	–
Kim et al. FV IBM [26]	1.09	–	–
Fadlun et al. [14]	1.08	–	–
$Re = 300$			
rSPH-IB (M =0.1)	0.71	0.062	0.133
Johnson and Patel [23]	0.66	0.069	0.137
Kim et al. FV IBM [26]	0.66	0.067	0.134
Ploumhans et al. [44]	0.68	0.066	0.137

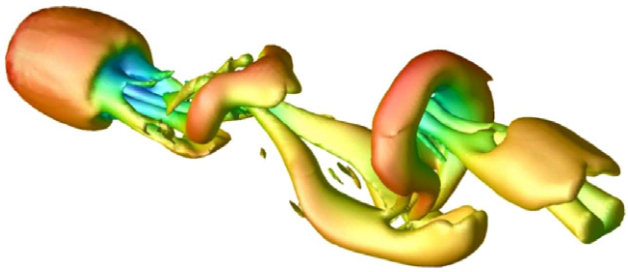

Fig. 9. Flow past a sphere at $Re = 300$. The vortices behind the sphere are visualized using the λ_2 method [22]. The color represent the local flow velocity.

Table 3
Falling sphere: Convergence study of the falling velocity

Particle spacing (h) ($\Delta t = 0.001$)	Falling velocity (t = 10)	Time step Δt ($h = 1/16$)	Falling velocity (t = 2)
1/8	1.02	0.004	0.602
1/16	0.95	0.002	0.592
1/32	0.93	0.001	0.596
Johnson et al. [23]	1.00	0.0005	0.595

lations using incompressible fluids. The domain size is $10d \times 10d \times 15d$, the particle spacing $h = 0.052d$ where d is the diameter of the sphere. The spacing of the boundary points is in average the same. The time integrator is Runge Kutta 4 using a time step of $\Delta t = 0.001$. Fig. 9 shows the three-dimensional vorticity structure at $Re = 300$. The surface of the vortices is identified by the λ_2 method of Jeong and Hussain [22]. At $Re = 300$ the flow is unsteady and the vortices shed asymmetrically. This flow behavior matches with the results of Johnson and Patel [24]. The agreement in the flow structure, as well as in the drag and lift coefficients indicate that the present method accurately captures the three-dimensional vorticity field.

4.4. Falling sphere

As a first test of flow-structure interaction we consider the problem of a falling sphere. We consider a rigid sphere of density $\rho_s = 1.041 > \rho_0$ at Reynolds number $Re = 100$ and at Mach number of $M = 0.25$. The sphere is released from rest and accelerates until it reaches its asymptotic falling velocity. The sphere diameter d is set to $d = 1$ and the gravity $g = 20$. The size of the domain is set to $6 \times 20 \times 6$, the time integration is Runge Kutta 2nd order with a time step of $\Delta t = 0.001$. Remeshing is applied every time step. An asymptotic falling velocity of $U = 0.95$ is reached at time $t = 10$ using a particle spacing of $1/16$. Table 3 summarizes the results of the falling sphere. This velocity of the falling sphere is in good agreement with the results from incompressible simulations reported by Johnson and Patel [23]. We note that by refining in space and time the falling velocity deviates from the reference value an effect that may be attributed to the compressibility of the flow in the present simulations. The computational time for one timestep using 750,000 particles is 28s on 2 CPUs of 2.2 GHz Opteron processors.

5. Simulation of anguilliform swimming

We present two and three-dimensional simulations of the proposed rSPH-IB methodology in flows past self-propelled anguilliform swimmers. Anguilliform swimmers, such as the eel and the lamprey, propel themselves by propagating curvature waves along their body and they are considered as highly efficient swimming organisms. The results are compared with related incompressible flow simulations using finite volume simulations and body-conforming grids presented by Kern et al. [25].

5.1. Fish geometry

The motion of the body is described by the two-dimensional deformation of the mid-line based on the simulations of Carling et al. [4]. The lateral displacement of the mid-line $y_s(s,t)$ in a local system is defined as

$$y_s(s,t) = 0.125\frac{s/L + 0.03125}{1.03125}\sin(2\pi(s/L - t/T)) \tag{34}$$

where s is the arc length along the mid-line of the body ($0 \leqslant s \leqslant L$), t is the time, T the periodic time.

The three dimensional body of the swimmer is described by spatially varying ellipsoid cross sections. The length of the two half axis $w(s)$ and $h(s)$ are defined as

$$w(s) = \begin{cases} \sqrt{2w_h s - s^2} 0 \leqslant s \leqslant s_b \\ w_h - (w_h - w_t)\left(\frac{s-s_b}{s_t-s_b}\right)^2 s_b \leqslant s \leqslant s_t \\ w_t \frac{L-s}{L-s_t} s_t \leqslant s \leqslant L \end{cases} \tag{35}$$

$$h(s) = b\sqrt{1 - \left(\frac{s-a}{a}\right)^2} \tag{36}$$

where $w_h = s_b = 0.04L$, $s_t = 0.95L$, $w_t = 0.01L$, $a = 0.51L$ and $b = 0.08L$. We apply a no-slip boundary condition on the surface of the body. The mid-line of the body is embedded into a non-inertial (x', y')-system where the center of mass of the deforming body remains and the total angular momentum is conserved. The fluid-body interactions are computed in the inertial system (x,y,z) considering the swimmer as a rigid body. Thus, the motion of the body in the global system (O, x, y, z) is described by the Newtons equations of motion:

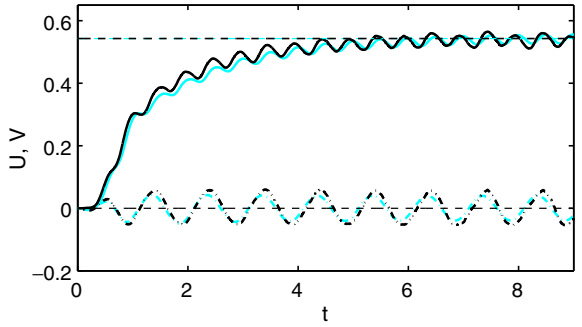

Fig. 10. Longitudinal (solid line) and lateral velocity (dashed line) of the two dimensional swimmer compared to finite volume solution (light blue or gray, respectively) [25]. (For interpretation of the references to colour in this figure legend, the reader is referred to the web version of this article.)

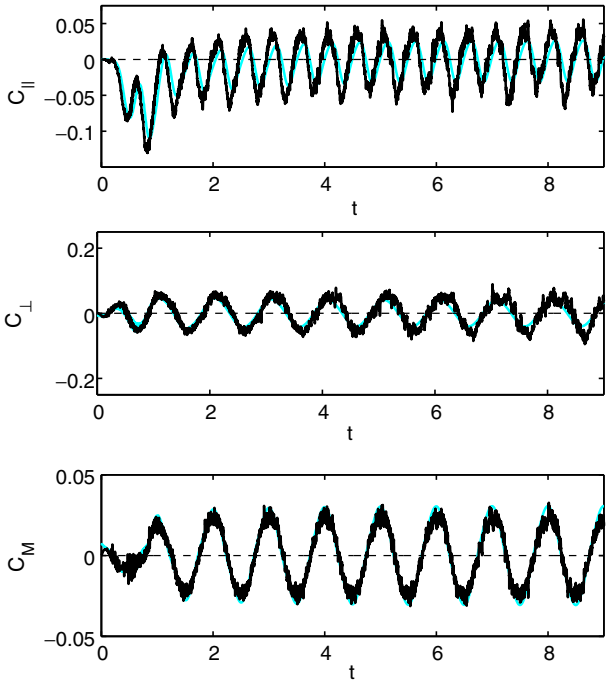

Fig. 11. Longitudinal force $C_\parallel$, lateral force $C_\perp$ and torque C_M of the two dimensional swimmer (black) compared to finite volume solution (light blue or gray, respectively) [25]. (For interpretation of the references to colour in this figure legend, the reader is referred to the web version of this article.)

$$m\ddot{x}_c = F, \tag{37}$$

$$\dot{I}_z\dot{\varphi}_c + I_z\ddot{\varphi}_c = M_z, \tag{38}$$

where m is the total mass of the immersed body, x_c represents the position of the center of mass, φ_c the global angle with respect to the initial position, F and M_z are the fluid force and yaw torque acting on the body surface. The time-dependency of the inertial moment $\dot{I}_z$ about the yaw axis is also considered although it is small compared to the inertial moment itself.

We set the viscosity of the fluid to be $\mu = 1.4 \times 10^{-4}$, the body length $L = 1$, the density $\rho_{0,\text{fluid}} = \rho_{\text{body}} = \rho = 1$ resulting in a Reynolds number of 3850 based on the final swimming speed.

The fluid forces acting on the body are shown as non-dimensional coefficients $C_\parallel = F_\parallel/(0.5\rho U_0^2 S)$ and $C_\perp = F_\perp/(0.5\rho U_0^2 S)$ parallel and lateral to the swimming direction, where S represents the circumference in two-dimensions and the surface of the body in three dimensions. The yaw torque is measured in the non-dimensional coefficient $C_M = M_z/(0.5\rho U_0^2 LS)$.

5.2. Equations of motion for the anguilliform swimmer

The position $\mathbf{x}_c$ and the angle φ_c of anguilliform swimmer evolve by the following set of equations based on Eqs. (37) and (38)

$$\begin{aligned}
\frac{d\mathbf{x}_c}{dt} &= \mathbf{u}_c,\\
\frac{d\mathbf{u}_c}{dt} &= \frac{\boldsymbol{F}}{m},\\
\frac{d\varphi_c}{dt} &= \omega_c,\\
\frac{d\omega_c}{dt} &= \frac{M_z - \dot{I}_z\omega_c}{I_z},
\end{aligned} \tag{39}$$

where u_c denotes the velocity of the swimmer and ω_c the angular velocity. We solve this set of equations simultaneously with the particle equations Eqs. ((26)–(31)) that describe the fluid behavior.

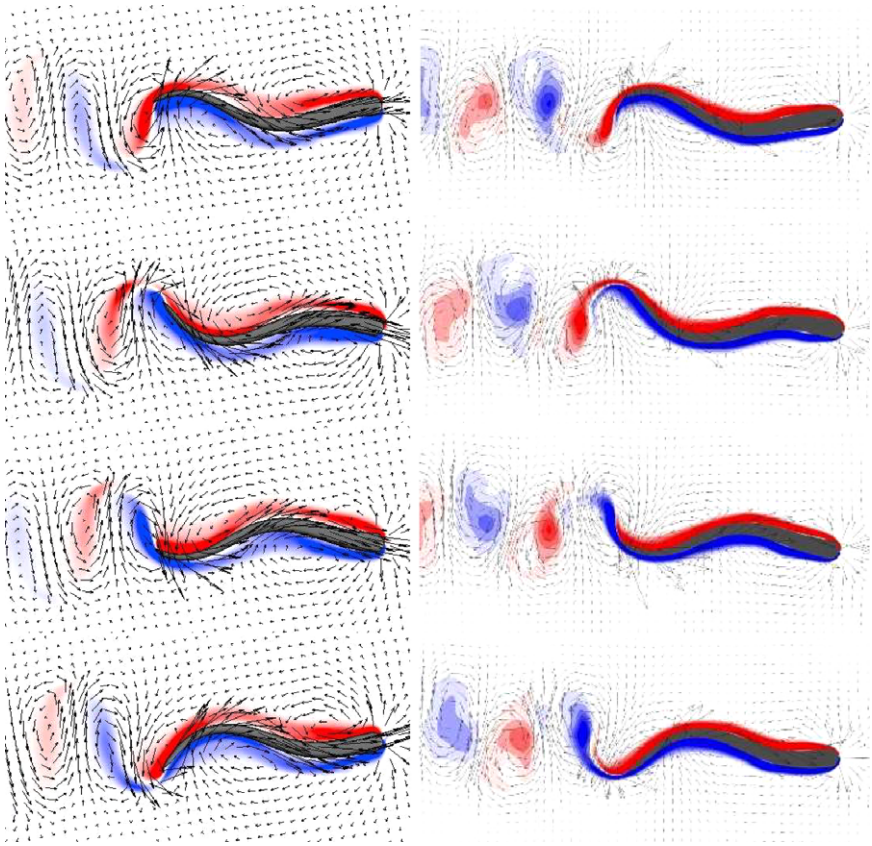

Fig. 12. Vorticity field of the two-dimensional swimmer using rSPH-IB (left) and reference solution of Kern [25] (right) for one swimming cycle at time t, $t + 0.25T$, $t + 0.5T$, and $t + 0.75T$.

5.3. Computational setup

We integrate the Eqs. (26)–(31), and (39) with respect to time using a explicit 4th order Runge-Kutta scheme with time step of $\Delta t = 0.001$. The particles are distributed uniformly in the domain and remeshed every time step. We consider the domain as an noninertial coordinate system that moves with the opposite x_1-component of the fish velocity such that x_1-position of the fish is constant in the noninertial coordinate system. Thus, we accelerate the fluid in x_1-direction by the opposite force that acts on the swimmer and the swimmer remains on its x_1-position. The size of the domain is 4×2 in two dimensions and $3 \times 2 \times 2$ in three dimensions. This domain size is tested to be sufficiently large to make negligible the influence of the boundary. The simulations are based on 1.3×10^5 particles in two dimensions, and 25×10^6 particles in three dimensions.

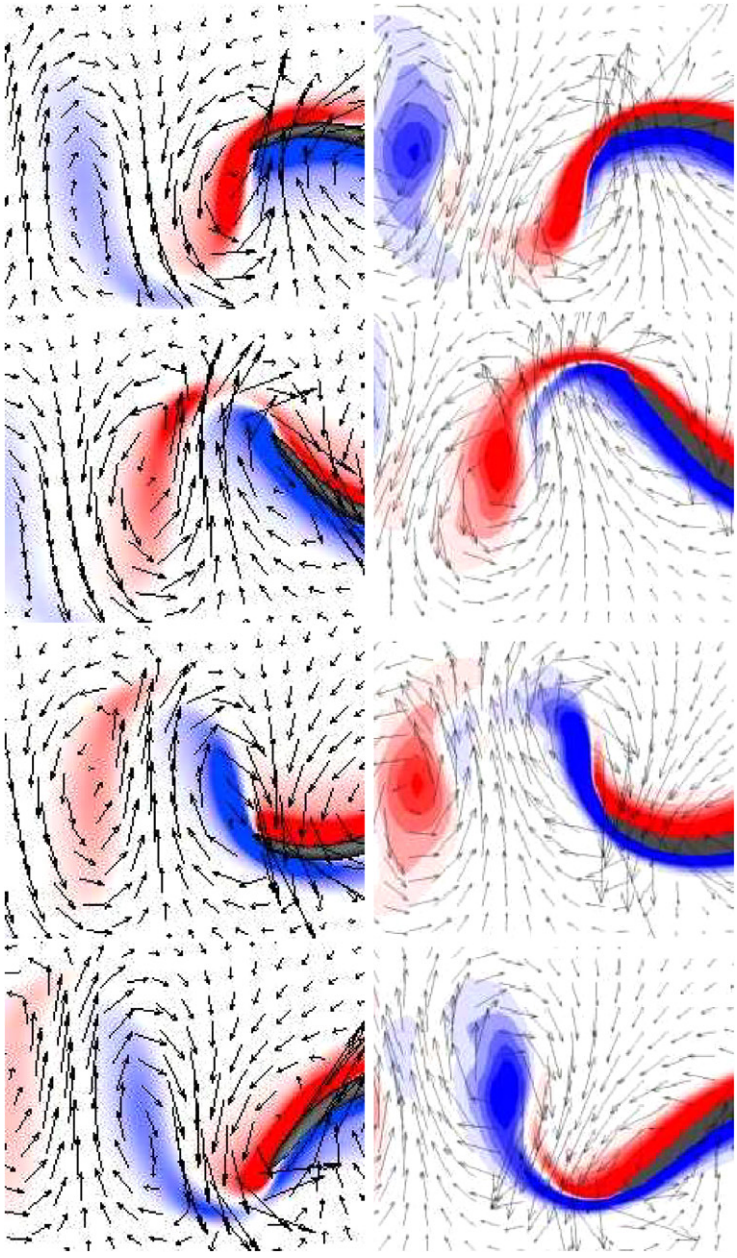

Fig. 13. Zoom of the vorticity field at the tail of the two-dimensional swimmer using rSPH-IB (left) and reference solution of Kern [25] (right) for one swimming cycle at time t, $t + 0.25T$, $t + 0.5T$, and $t + 0.75T$.

5.4. Results

5.4.1. Two-dimensional anguilliform swimmer

We present a comparison in the two dimensional flows with the work of Kern et al. [25] in terms of the swimming velocity, as well as forces and torque acting on the swimmer. The swimmer accelerates from rest to an asymptotic mean forward velocity of $\overline{U}_{\parallel} = 0.54$ in about seven undulation cycles. The velocity varies slightly during a cycle while the lateral velocity $U_{\perp}$ has an amplitude of 0.04. The time history of the longitudinal and lateral velocity agrees very well with the incompressible solution (Fig. 10). The velocity differs the most at time $1 < t < 4$ where the density variations are larger than at later time steps. The higher density variations lead to higher pressure variations resulting in larger forces acting on the swimmer. The incompressible solution is approximated sufficiently with a Mach number of $M = 0.1$.

The longitudinal and lateral forces and the torque (Fig. 11) agree very well with the incompressible solution. The force and moment coefficient $C_{\parallel}, C_{\perp}$ and C_M converge to oscillation modes with zero mean and a constant amplitude of 0.03, 0.04 and 0.03, respectively. After the body has accelerated to its mean swimming velocity the forces acting on the body have a zero mean. The computation of one time step took 10s on 8 processors for 800,000 particles.

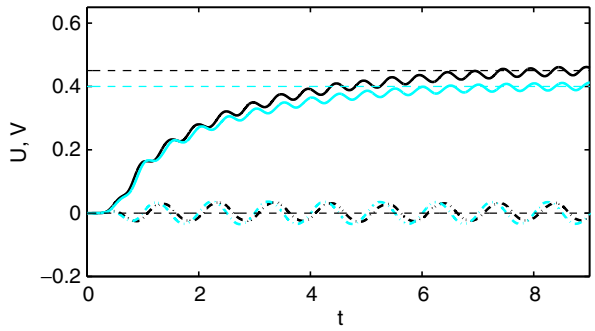

Fig. 14. Longitudinal (solid line) and lateral velocity (dashed line) of the three dimensional swimmer compared to finite volume solution (light blue or gray, respectively) [25]. (For interpretation of the references to colour in this figure legend, the reader is referred to the web version of this article.)

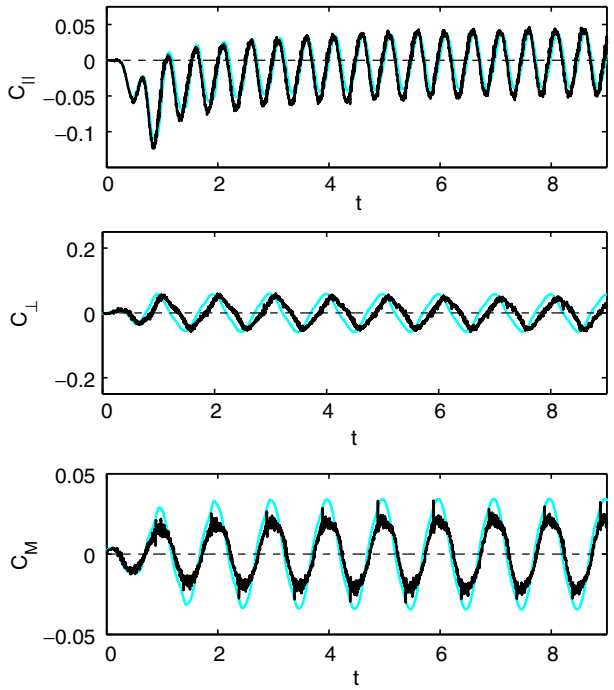

Fig. 15. Longitudinal force $C_{\parallel}$, lateral force $C_{\perp}$ and torque C_M of the three dimensional swimmer (black) compared to finite volume solution (light blue or gray, respectively) [25]. (For interpretation of the references to colour in this figure legend, the reader is referred to the web version of this article.)

The compressibility of the fluid causes unresolved pressure waves resulting in high frequent noise in the flow structure. A second order filter [43] is applied to the mass and the momentum during the remeshing process every 100 steps to suppress the small scale pressure waves in the range of the Nyquist frequency. We note that Kern et al. [25] applied a low pass filter to the fluid force F and the torque M_z in order to stabilize the simulation of the incompressible flow. In the present method the flow-structure is stable and we can omit the use of such a low pass filter.

Figs. 12 and 13 show the vorticity field of the swimmer during one period at the final swimming speed along with a zoom at the tail. The main differences in the vorticity field result from the fact that the particle solution is uniformly resolved, whereas the finite volume solution involves an adaptive re-gridding. Thus, the vorticity shedding at the boundary layer is better resolved in the finite volume solution.

The tail beat amplitude is $A = 0.16$ and the corresponding Strouhal number is $St = 0.59$. The wave velocity is $V = 0.73$, which results in a slip of $\overline{U}_{\parallel}/V = 0.74$.

5.4.2. Three-dimensional anguilliform swimmer

In three dimensions the forces acting on the fish compare well with the finite volume solution (Fig. 15). The net force and moment coefficient $C_{\parallel}, C_{\perp}$ and C_M oscillate with a mean of zero and amplitudes of 0.04, 0.06 and 0.03, respectively. Fig. 14 shows that the final swimming speed in the particle solution ($u_{SPH} = 0.448$) is 12% higher than the velocity reported in the finite volume solution ($u_{FV} = 0.402$). This result is consistent with the drag values reported in the flow past a sphere at $Re = 300$ that were found to differ approximately 10% from the results of grid based methods (Table 2). The forward velocity $U_{\parallel}$ oscillates with an amplitude of 0.01. The lateral velocity $U_{\perp}$ has a zero mean and an amplitude of 0.03 (Fig. 14). The wave velocity $V = 0.73$ is equal to the two dimensional case resulting in the slip of $\overline{U}_{\parallel}/V = 0.61$. The tail beat amplitude is determined to be $A = 0.15$ with $St = 0.67$.

The oscillating tail of the swimmer sheds vortex rings in the wake with the frequency of the swimming motion (Figs. 16–18). Both, the particle and the finite volume solution show the vorticity shed in every half tail beat cycle that breaks up into two vortices resulting in near wake lateral jets. The vorticity field of particle solution appears smoother and shows less small-scale structures. The vortex rings are less recognizable. As the finite-volume grid feature a four times higher resolution

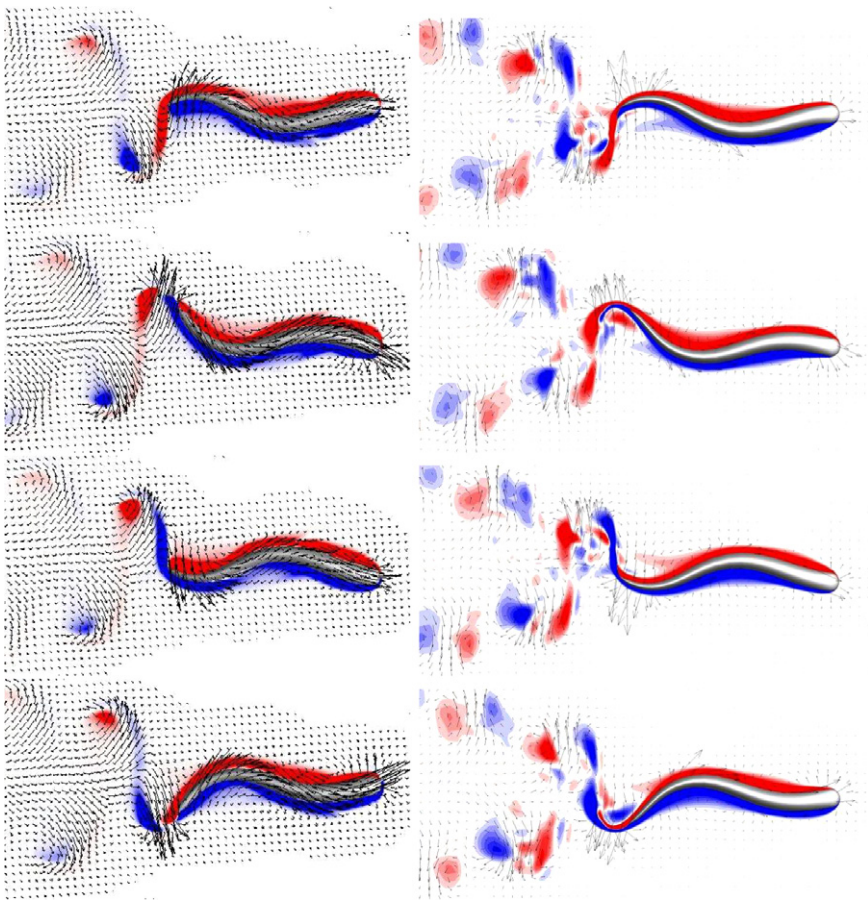

Fig. 16. Vorticity field of the three-dimensional swimmer using rSPH-IB (left) and reference solution of Kern [25] (right) for one swimming cycle at time t, $t + 0.25$T, $t + 0.5$T, and $t + 0.75$T.

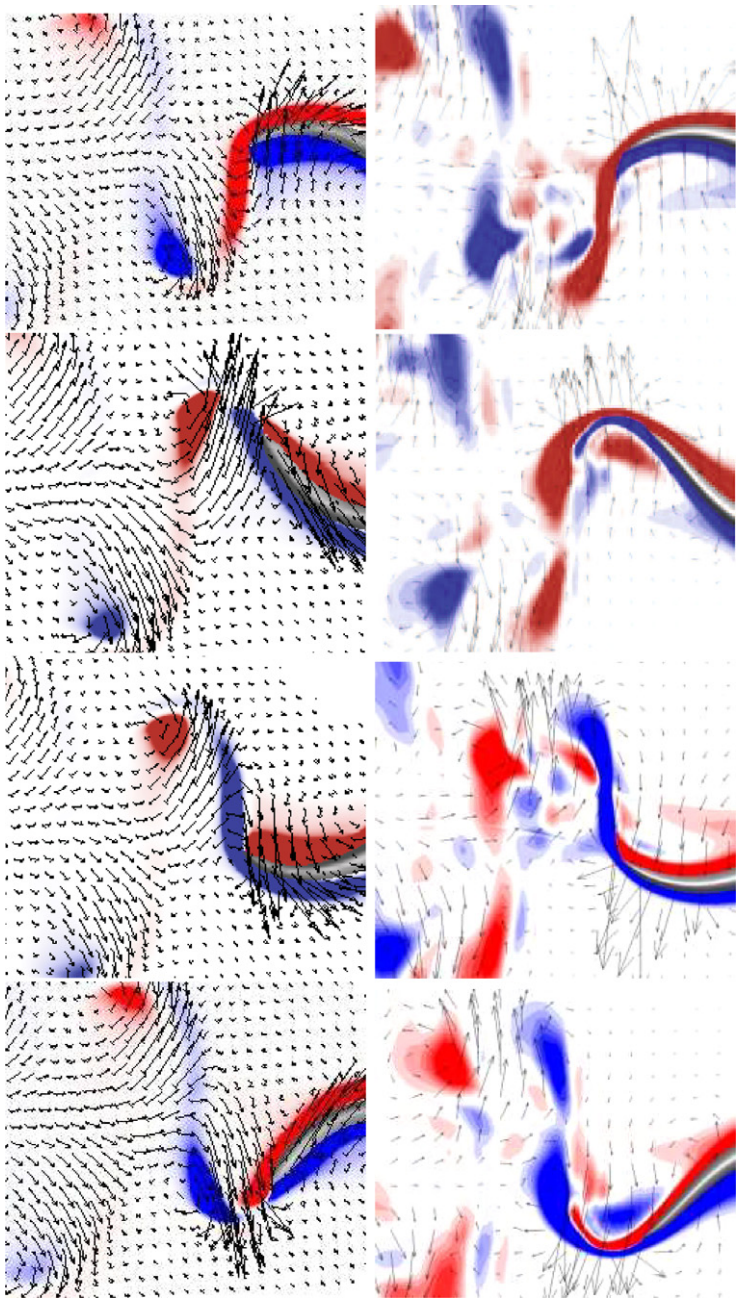

Fig. 17. Zoom of the vorticity field at the tail of the three-dimensional swimmer using rSPH-IB (left) and reference solution of Kern [25] (right) for one swimming cycle at time t, $t + 0.25T$, $t + 0.5T$, and $t + 0.75T$.

in the boundary layer of the tail than the particle solution, the absence of the small-scale structures in the boundary layer can be associated with a lack of resolution. The small vorticity structures between the shedding vortex pair result are mainly spurious and result from the highly dynamic refinement of the finite volume grid. The computation of one time step took 70s on 32 processors for 13 million particles.

6. Conclusion

We presented a novel particle method (rSPH-IB) for simulations of flow-structure interactions involving unsteady deforming geometries. The present method combines a Level Set technique for the implicit representation of the body, along with a remeshed Smoothed Particle Hydrodynamics solver for the simulation of the flow field and an Immersed Boundary method to enforce the no-slip boundary condition. The present method relies on the remeshing of the Lagrangian particles

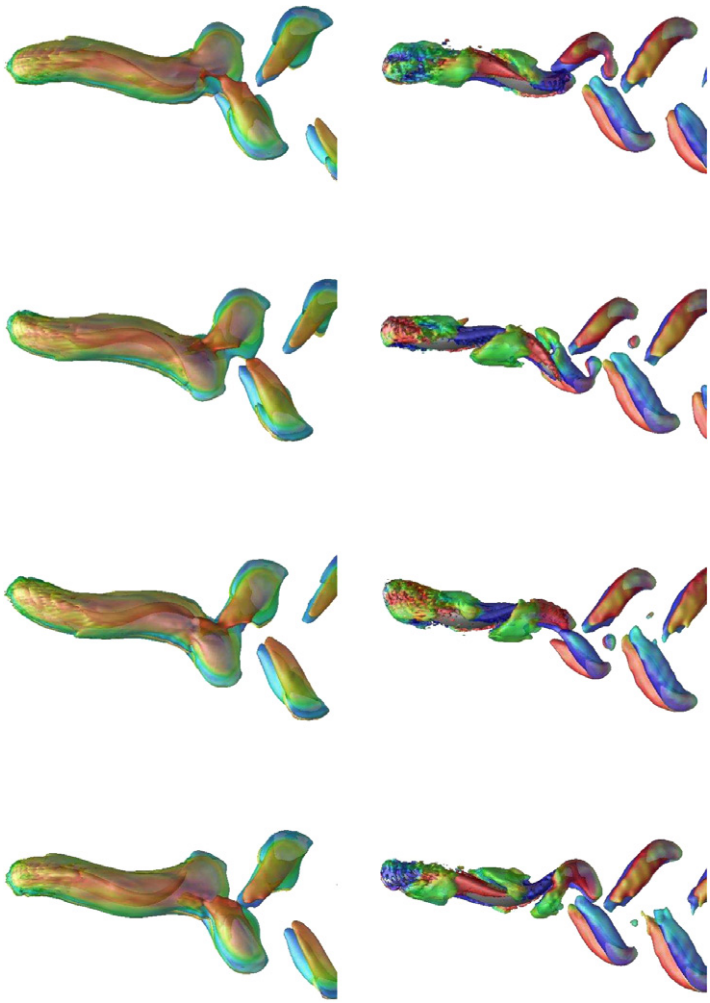

Fig. 18. Isosurface of the vorticity magnitude (left) and vortices visualized by the λ_2-method (right) of the three-dimensional swimmer using rSPH-IB for one swimming cycle at time t, $t + 0.25T$, $t + 0.5T$, and $t + 0.75T$.

on a rectangular grid. This remeshing does not detract from the adaptive character of the method as the particles adapt to resolve the flow field and at the same time it ensures the convergence of the method when the particles get distorted by the flow map. The efficiency and accuracy of the method, as well as comparison with related methodologies, is demonstrated in a number of two and three dimensional benchmark problems and the method is shown to be well capable in solving problems of fluid-structure interaction. The simplicity of the method in handling complex boundaries makes it suitable for large scale simulations, employing millions of particles for the simulation of complex movement of flexible structures as they appear for example in anguilliform swimming. A drawback of the present method is the need to account for the compressibility of the flow. Fast motions of the boundary in high Reynolds number flows result in pressure waves in the fluid that restrict the time step and can lead to numerical problems when not properly resolved. The use of artificial damping terms may help to remedy the situation much as it is the case in artificial compressibility methods. Another limitation of the present rSPH-IB formulation is the use of a uniform particle size throughout the computational domain. We are currently addressing this inefficiency of the method by incorporating multi-resolution particle techniques [2,3] and developing its implementation on GPUs following related work on Vortex Methods [46]. The present method allows for simulations past complex deforming geometries, while the level set description of the surface enables flow simulations even past bodies that undergo topological changes. We pursue applications of this method to other problems related to swimming and flying in nature, as well as to simulations of flow-structure interaction as they pertain to virtual surgery.

Acknowledgment

We would like to thank Dr. Stefan Kern (ETHZ) and Prof. Tony Leonard (Caltech) for several helpful discussions throughout this work. We wish to acknowledge several helpful interactions with Caroline Hieber during the writing of this paper.

This project was funded by the Swiss National Science Foundation, NCCR' Computer Aided and Image Guided Medical Interventions' (Co-Me).

References

[1] J.T. Beale, A convergent 3-D vortex method with grid-free stretching, Math. Comput. 46 (1986) 401–424.
[2] M. Bergdorf, G.-H. Cottet, P. Koumoutsakos, Multilevel adaptive particle methods for convection-diffusion equations, Multiscale Model. Simul. 4 (1) (2005) 328–357.
[3] M. Bergdorf, P. Koumoutsakos, A lagrangian particle-wavelet method, Multiscale Model. Simul. 14 (2006) 980–995.
[4] John Carling, Thelma L. Williams, Graham Bowtell, Self-propelled anguilliform swimming: simultaneous solution of the two-dimensional Navier–Stokes equations and Newtons' laws of motion, J. Exp. Biol. 201 (1998) 3143–3166.
[5] A.K. Chaniotis, D. Poulikakos, P. Koumoutsakos, Remeshed smoothed particle hydrodynamics for the simulation of viscous and heat conducting flows, J. Comput. Phys. 182 (1) (2002) 67–90.
[6] A.J. Chorin, Numerical study of slightly viscous flow, J. Fluid Mech. 57 (4) (1973) 785–796.
[7] G.-H. Cottet, Artificial viscosity models for vortex and particle methods, J. Comput. Phys. 127 (1996) 299–308.
[8] G.-H. Cottet, P. Koumoutsakos, Vortex Methods – Theory and Practice, Cambridge University Press, New York, 2000.
[9] Georges-Henri Cottet, Bertrand Michaux, Sepand Ossia, Geoffroy VanderLinden, A comparison of spectral and vortex methods in three-dimensional incompressible flows, J. Comput. Phys. 175 (2002) 702–712.
[10] G.H. Cottet, E. Maitre, A level set method for fluid-structure interactions with immersed surfaces, Mathematical Models and Methods in the Applied Sciences 16 (2006) 415–438.
[11] P. Degond, S. Mas-Gallic, The weighted particle method for convection-diffusion equations. Part 1: The case of an isotropic viscosity, Math. Comput. 53 (188) (1989) 485–507.
[12] A. Dupuis, P. Chatelain, P. Koumoutsakos, An immersed boundary-lattice boltzmann method for the simulation of the flow past an impulsively started cylinder, J. Comput. Phys. 227 (9) (2008) 4486–4498.
[13] Jeff D. Eldredge, Anthony Leonard, Tim Colonius, A general determistic treatment of derivatives in particle methods, J. Comput. Phys. 180 (2) (2002) 686–709.
[14] E.A. Fadlun, R. Verzicco, P. Orlandi, J. Mohd-Yusof, Combined immersed-boundary finite-difference methods for three-dimensional complex flow simulations, J. Comput. Phys. 161 (1) (2000) 35–60.
[15] C. Farhat, M. Lesoinne, Automatic partitioning of unstructured meshes for the parallel solution of problems in computational mechanics, Int. J. Numer. Methods Eng. 36 (5) (1993) 745.
[16] Bengt Fornberg, Steady viscous flow past a sphere at high Reynolds numbers, J. Fluid Mech. 190 (1988) 471–489.
[17] R.A. Gingold, J.J. Monaghan, Smoothed particle hydrodynamics: theory and application to non-spherical stars, Month Notices Roy. Astron. Soc. 181 (1977) 375–389.
[18] Ole H. Hald, Convergence of vortex methods for Euler's equations, III, SIAM J. Numer. Anal. 24 (3) (1987) 538–582.
[19] R.D. Henderson, Details of the drag curve near the onset of vortex shedding, Phys. Fluids 7 (1995) 2102–2104.
[20] S.E. Hieber, J.H. Walther, P. Koumoutsakos, Remeshed smoothed particle hydrodynamics simulation of the mechanical behavior of human organs, J. Technol. Health Care 12 (4) (2004) 305–314.
[21] Simone Elke Hieber, Petros Koumoutsakos, A Lagrangian particle level set method, J. Comput. Phys. 210 (2005) 342–367.
[22] H. Jeong, B. Tombor, R. Albert, Z.N. Oltvai, A.-L. Barabási, The large-scale organization of metabolic networks, Nature 407 (2000) 651–654.
[23] A.T. Johnson, V.C. Patel, Flow past a sphere up to a Reynolds number of 300, J. Fluid Mech. 378 (1999) 19–70.
[24] Gordon R. Johnson, Robert A. Stryk, Stephen R. Beissel, SPH for high velocity impact computations, Comput. Meth. Appl. Mech. Eng. 139 (1996) 347–373.
[25] Stefan Kern, Petros Koumoutsakos, Simulations of optimized anguilliform swimming, J. Exp. Biol. 209 (2006) 4841–4857.
[26] Jungwoo Kim, Dongjoo Kim, Haecheon Choi, An immersed-boundary finite-volume method for simulations of flow in complex geometries, J. Comput. Phys. 171 (2001) 132–150.
[27] P. Koumoutsakos, Inviscid axisymmetrization of an elliptical vortex ring, J. Comput. Phys. 138 (1997) 821–857.
[28] P. Koumoutsakos, Vorticity flux control in a turbulent channel flow, Phys. Fluids 11 (2) (1999) 248–250.
[29] P. Koumoutsakos, Multiscale flow simulations using particles, Annu. Rev. Fluid Mech. 37 (2005) 457–487.
[30] P. Koumoutsakos, A. Leonard, High-resolution simulation of the flow around an impulsively started cylinder using vortex methods, J. Fluid Mech. 296 (1995) 1–38.
[31] A. Leonard, Review. vortex methods for flow simulation, J. Comput. Phys. 37 (1980) 289–335.
[32] A.L.F. Lima E Silva, A. Silveira-Neto, J.J.R. Damasceno, Numerical simulations of two-dimensional flows over a circular cylinder using the immersed boundary method, J. Comput. Phys. 189 (2003) 351–370.
[33] L.B. Lucy, A numerical approach to the testing of the fission hypothesis, Astron. J. 82 (1977) 1013–1024.
[34] Rajat Mittal, Gianluca Iaccarino, Immersed boundary methods, Annu. Rev. Fluid Mech. 37 (2005) 239–261.
[35] J.J. Monaghan, Smoothed particle hydrodynamics, Annu. Rev. Astron. Astrophys. 30 (1992) 543–574.
[36] J.J. Monaghan, Smoothed particle hydrodynamics, Rep. Progress Phys. 68 (8) (2005) 1703–1759.
[37] G. Morgenthal, J.H. Walther, An immersed interface method for the vortex-in-cell algorithm, Comput. Struct. 85 (2007) 712–726.
[38] J. Park, K. Kwon, H. Choi, Numerical solutions of flow past a cylinder at Reynolds number up to 160, KSME Int. J. 12 (6) (1998) 1200–1205.
[39] Charles Peskin, Flow patterns around heart valves: A numerical study, J. Comput. Phys. 10 (1972) 252–271.
[40] C.S. Peskin, Numerical analysis of blood flow in the heart, J. Comput. Phys. 25 (1977) 220–252.
[41] C.S. Peskin, The immersed boundary method, Acta Numer. 11 (2002) 479–517.
[42] C.S. Peskin, D.M. McQueen, Modeling prosthetic heart-valves for numerical analysis of blood flow in the heart, J. Comput. Phys. 37 (1980) 113–132.
[43] Roger Peyret, Thomas Taylor, Computational Methods for Fluid Flow, Springer-Verlag, 1983.
[44] P. Ploumhans, G.S. Winckelmans, J.K. Salmon, A. Leonard, M.S. Warren, Vortex methods for direct numerical simulation of three-dimensional bluff body flows: Applications to the sphere at $Re = 300$, 500 and 1000, J. Comput. Phys. 178 (2002) 427–463.
[45] Anatol Roshko, Experiments on the flow past a circular cylinder at very high Reynolds number, J. Fluid Mech. 10 (3) (1961) 345–356.
[46] Diego Rossinelli, Petros Koumoutsakos, Vortex methods for incompressible flow simulations on the GPU, Visual Comput. 12 (2008).
[47] I.F. Sbalzarini, J.H. Walther, M. Bergdorf, S.E. Hieber, E.M. Kotsalis, P. Koumoutsakos, PPM – a highly efficient parallel particle-mesh library for the simulation of continuum systems, J. Comput. Phys. 215 (2006) 566–588.
[48] S.P. Singh, S. Mittal, Flow past a cylinder: shear layer instability and drag crisis, Int. J. Numer. Methods Fluids 47 (2005) 75–98.
[49] Xiaodong Wang, Wing Kam Liu, Extended immersed boundary method using fem and rkpm, Comput. Methods Appl. Mech. Eng. 193 (12–14) (2004) 1305–1321.
[50] C.H.K. Williamson, Oblique and parallel modes of vortex shedding in the wake of a circular cylinder at low Reynolds numbers, J. Fluid Mech. 206 (1989) 579–627.